Progress In Electromagnetics Research C, Vol. 96, 27–41, 2019

Analysis and Experiment of a Ridged Horn Antenna with Metallic Grid Sidewalls

Shu Lin*, Shoulan Liu, Yuwei Zhang, and Jianlin Jiao

Abstract—A ridged horn antenna with metallic grid sidewalls is proposed and quantitatively analyzed. Simulated and measured results indicate that the operating band is from 1.0 to 20.0 GHz with the reflection coefficient less than −10 dB, and the relative bandwidth is as high as 180.95%. The gains are greater than 10 dBi in the frequency band of 2.6–20 GHz and greater than 16 dBi in the frequency band of 10–20 GHz with the gains fluctuation less than 1 dB. In the whole operating band, the radiation patterns radiate directionally along the normal direction of the horn aperture and do not split. In this paper, the ridged horn antenna with metallic girds is analyzed quantitatively. A modified equivalent traveling wave current model of the ridged horn antenna is proposed, which matches better to the patterns of the ridged horn antenna in high frequency band. The working mechanism of metallic grid sidewalls is also analyzed quantitatively, and the reason that metal strips can improve the matching performance of ridged horn antenna in low frequency band, restrain the patterns splitting in high frequency band, and improve the antenna gains is explained. The proposed antenna has the characteristics of ultra-wideband, stable gains, miniaturization, and directional radiation patterns with no splitting main lobe in ultra-wideband. The proposed ridged horn antenna can be used for the measurement in a microwave anechoic chamber.

1. INTRODUCTION

Ridged horn antenna is a directional radiation antenna with ultra-wideband (UWB) characteristics. Once proposed, it has attracted wide attention of researchers [1–4]. There are various forms of the ridged antenna in recent years [5–7]. Ridged TEM horn antenna is a typical example, which combines the two factors of wideband: ridge and TEM horn. In addition, the relative bandwidth can achieve 20 : 1 or more.

At present, the main problems of UWB ridged horn antenna are poor matching characteristics in low frequency band, splitting of patterns, and abrupt drop of gains in high frequency band. In view of these problems, the main methods adopted at present are improving the feed structure, such as loading wedge blocks [8, 9] proposed by Botello-Perez et al. and Abbas-Azimi et al. and adding some reflective structures [10] proposed by Rodriguez; improving the ridge structure, such as loading slot on the ridges and gradual widening structure of ridges [11]; removing the sidewalls of the horn [12, 13], loading metal strips [14]; loading lens [15]. Previous researchers mainly focused on the structure design of ridged antenna, but less on the working mechanism of antenna. Working mechanism was mentioned in [16–18], but with only qualitative analysis. In [14, 19–21], the design scheme of adding metallic strips to the sidewalls of the horn is proposed; however, there is no quantitative analysis of the working mechanism for the metal strips.

In this paper, a ridged horn antenna with metallic grid sidewalls is designed and fabricated, and its working mechanism is analyzed quantitatively. Modeling and simulation of antennas are carried out in CST Microwave Studio® software. Firstly, the TEM ridged horn antenna is designed. A modified

Received 15 July 2019, Accepted 4 September 2019, Scheduled 19 September 2019
* Corresponding author: Shu Lin (linshu@hit.edu.cn).
The authors are with the Harbin Institute of Technology, China.

equivalent traveling wave current model is proposed on basis of the previous paper [22] presented by the authors' team. The modified traveling wave current model reduces the error between the straight line and the exponential ridge curve. The radiation characteristics of the antenna are explained based on the modified model. Secondly, in order to effectively improve the matching characteristics in low frequency band and suppress splitting of radiation patterns in high frequency band of the TEM ridged horn antenna, several pairs of metal strips are added to the horn sidewalls. The working mechanism of metal strips is analyzed quantitatively. The reason that the matching performance of antenna is improved in low frequency band is explained from the angle of capacitance inductance resonance; the reason that metal strips restrain the splitting of patterns and improve antenna gains is explained from the angle of compensating radiation of dipole array. The simulation results are in good agreement with the calculation ones, which proves the correctness of the proposed model. Design of antenna structure and simulation results are depicted in Section 2; quantitative analysis of working mechanism based on equivalent models is presented in Section 3; prototype of the antenna and test results are displayed in Section 4, while the conclusions are provided in Section 5.

2. DESIGN OF ANTENNA STRUCTURE AND SIMULATION RESULTS

As shown in Figure 1, the TEM ridged horn antenna is designed by combining the two broadband factors: ridge and TEM horn. The design of the antenna is divided into three parts: parallel coaxial feeding part, the transition part between the feeding coaxial line and the ridged horn, and the ridged horn part. The UWB characteristics of the designed antenna are realized by using ridged waveguide and exponential ridge structure. The diagram of ridge curve is shown in Figure 2. The formula of the ridge curve is: $y = 0.5e^{0.022z} + 0.002z + 0.1$, unit: mm. The overall size of the antenna is: 240 mm × 140 mm × 94.6 mm.

The reflection coefficients of the TEM ridged horn antenna are shown in Figure 3. It can be seen

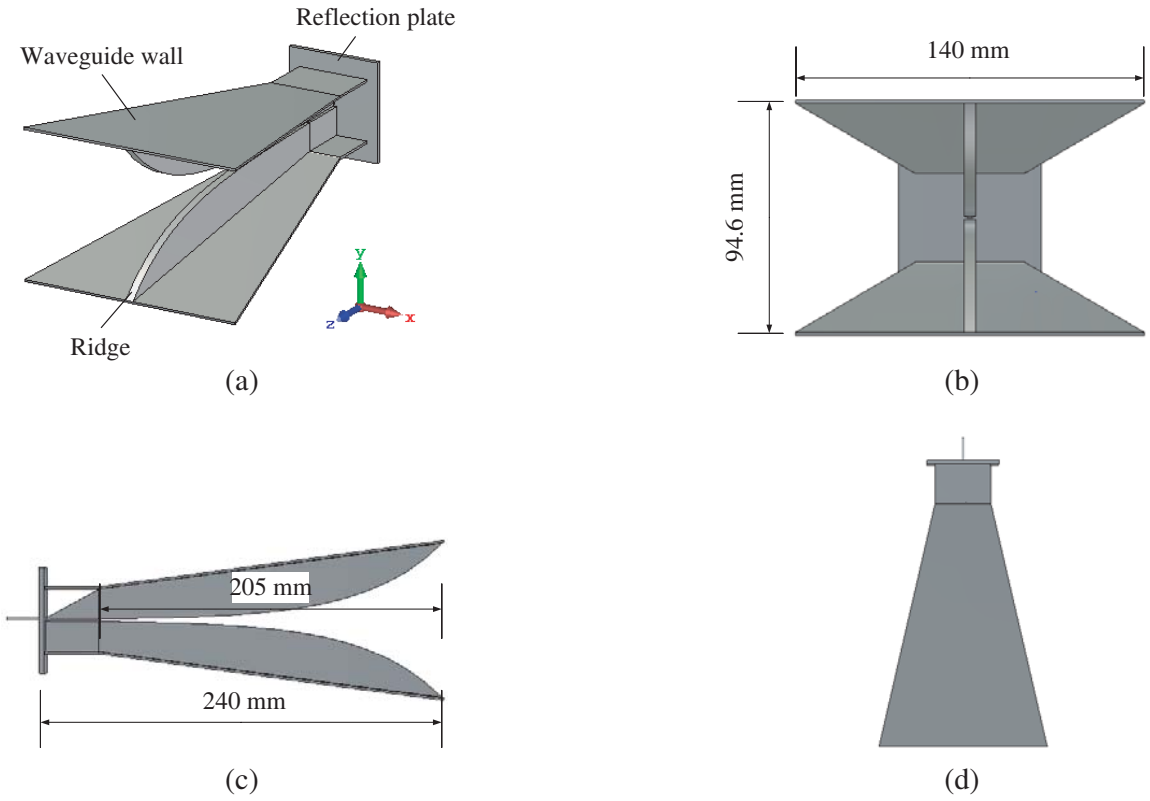

Figure 1. Geometry of ridged TEM horn antenna (antenna-1). (a) Perspective view. (b) Front view. (c) Side view. (d) Top view.

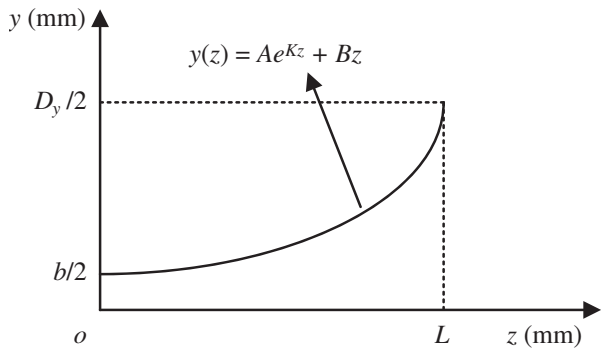

Figure 2. The general form of ridge curve (b is the distance between ridges, D_y is the height of the horn aperture, L is the length of the horn).

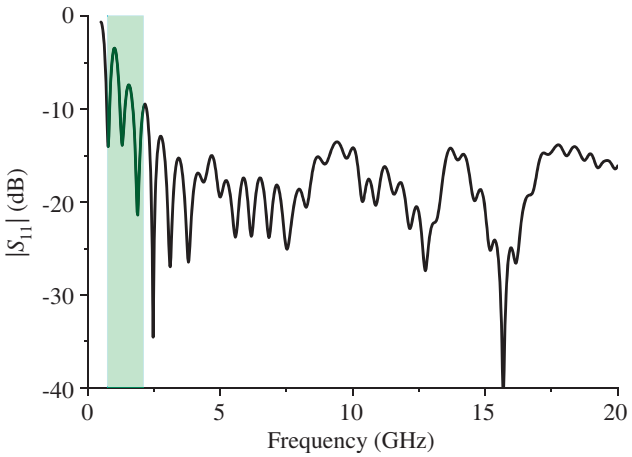

Figure 3. Reflection coefficients of the TEM ridged horn antenna.

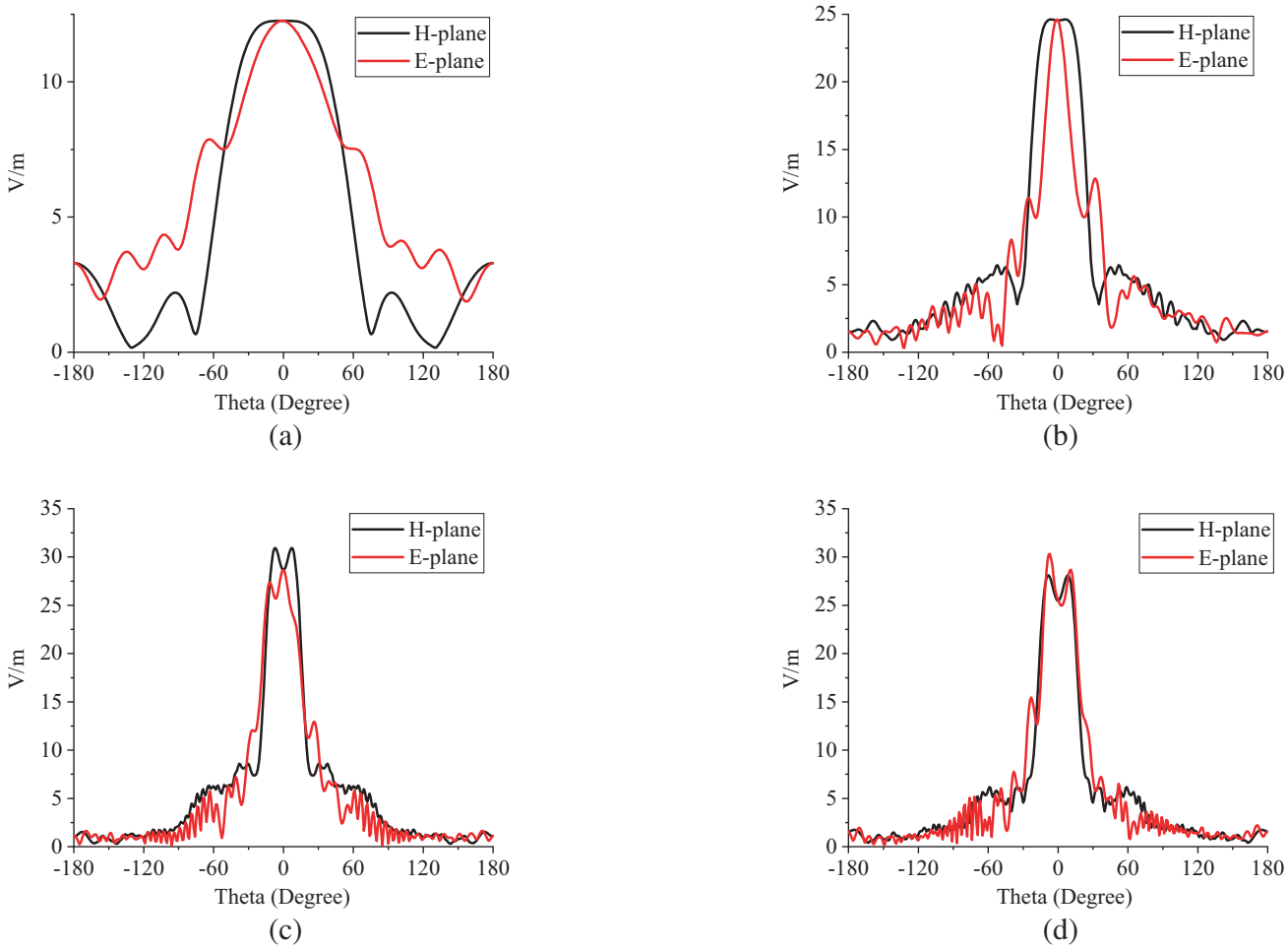

Figure 4. Patterns (arithmetic value of the electric field strength) of the ridged TEM horn antenna, (a) 2 GHz, (b) 8 GHz, (c) 16 GHz, (d) 18 GHz.

that the reflection coefficients of the antenna are less than −10 dB in the frequency band of 1.7 GHz–20 GHz. The reflection coefficients exhibit a state of oscillation in the frequency range of 1–1.7 GHz.

Figure 4 shows patterns of the ridged TEM horn antenna. The patterns here are drawn by the linear value of the electric field intensity. It should be noticed that H-plane patterns of the ridged horn antenna split obviously in high frequency band.

The simulation results demonstrate that the reflection coefficients of the TEM horn antenna oscillate obviously in the frequency range of 1–1.7 GHz, and the H-plane patterns split in high frequency band. To solve the above problems, it is necessary to improve the TEM ridged horn antenna. The TEM ridged horn antenna is linearly polarized (along the Y direction), and there is capacitance between the upper and lower walls of the TEM horn. In order to widen the bandwidth of antenna in low frequency band and restrain the splitting of patterns in high frequency band, several pairs of metal strips with the same polarization direction as the antenna's are introduced into the sidewalls of the TEM horn, which can provide compensating radiation for antenna and restrain the splitting of main lobe. At the same time, the metal strip can be regarded as an inductance structure, which can expand the bandwidth of the antenna by resonating with the capacitance structure on the sidewalls of TEM horn in low frequency band. Therefore, a ridged horn antenna with metallic grid sidewalls is proposed as shown in Figure 5.

Figure 6 illustrates the comparison results of the reflection coefficients between antenna-1 (without metallic grid sidewalls) and antenna-2 (with metallic grid sidewalls). Due to the introduction of metal strips, the oscillation of reflection coefficients in low frequency band disappears, and the −10 dB impedance bandwidth of antenna-2 is 1.0–20.0 GHz. The introduction of metal strips obviously improves

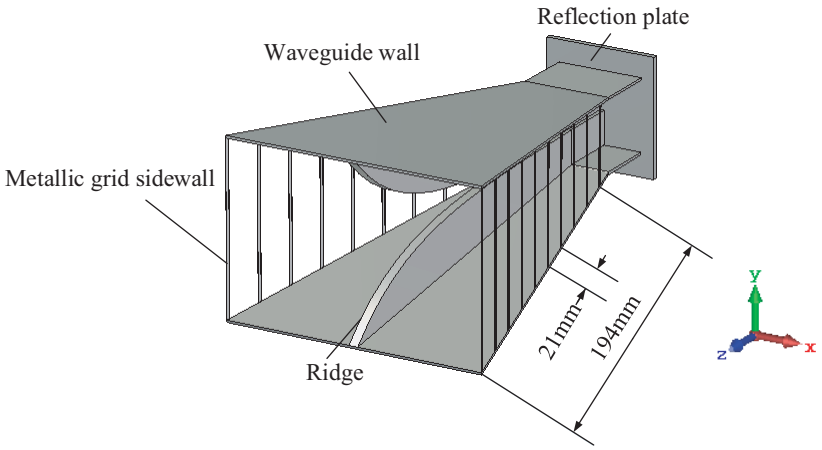

Figure 5. Ridged horn antenna with metallic grid sidewalls (antenna-2).

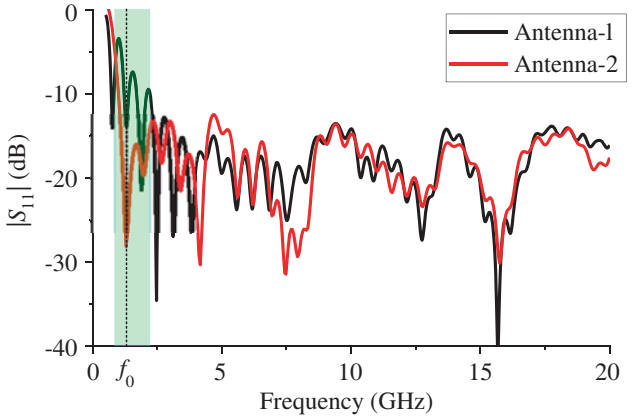

Figure 6. Comparison of reflection coefficients between antenna-1 and antenna-2.

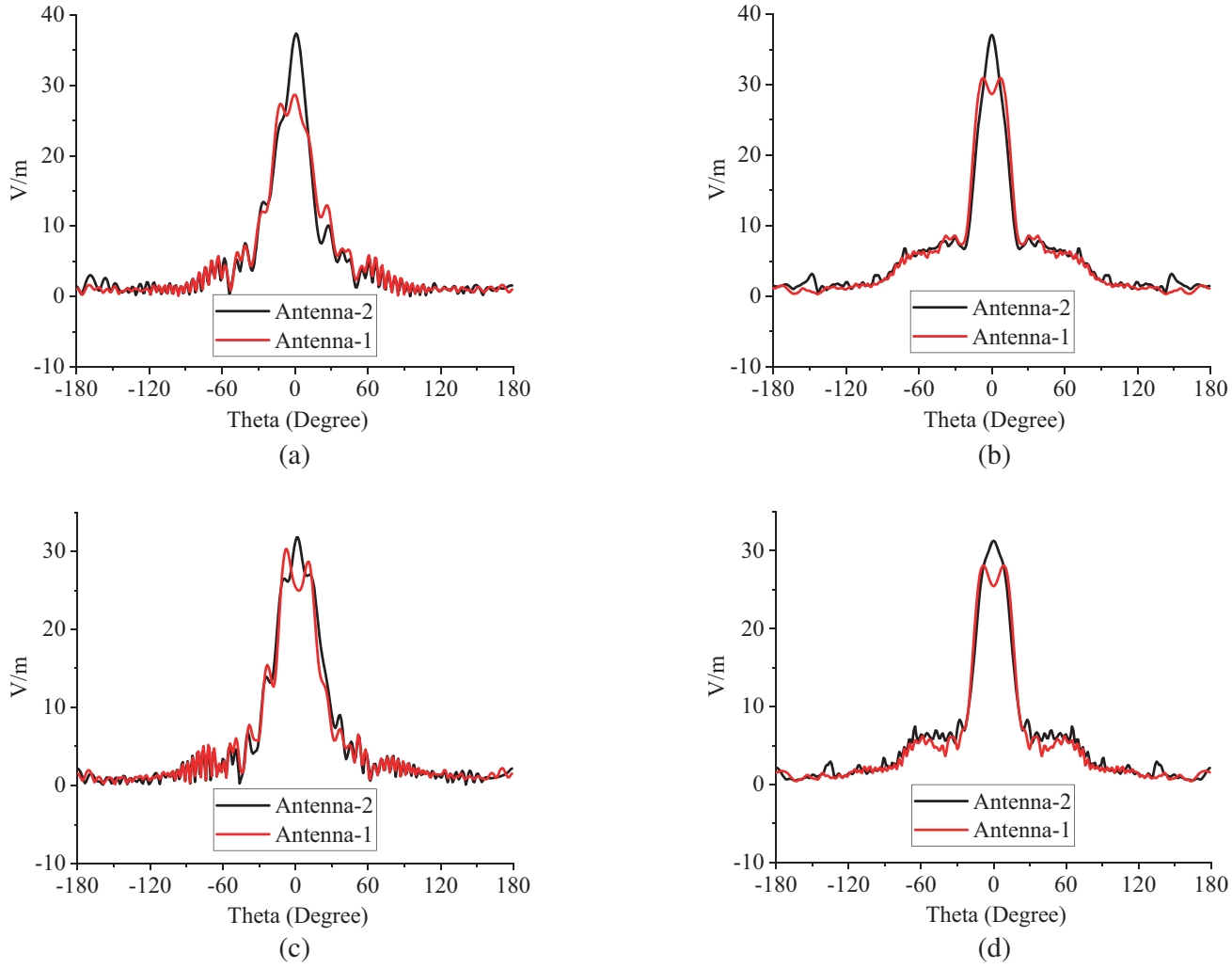

Figure 7. Comparison of electric field patterns (arithmetic) between antenna-1 and antenna-2. (a) 16 GHz/E-plane. (b) 16 GHz/H-plane. (c) 18 GHz/E-plane. (d) 18 GHz/H-plane.

the matching characteristics in low frequency band thus widening the bandwidth of the horn antenna.

Figure 7 illustrates the comparison of the electric field patterns (linear) between antenna-1 and antenna-2. It can be seen that the splitting of patterns in high frequency band is well suppressed due to the compensation radiation of the metal strips on the sidewalls of the horn.

Figure 8 shows the comparison results of gains between antenna-1 and antenna-2. It can be seen that due to the introduction of metal strips, the overall gains of antenna-2 are improved compared with those of antenna-1.

3. QUANTITATIVE ANALYSIS OF WORKING MECHANISM BASED ON EQUIVALENT MODELS

3.1. Proposal of a Modified Equivalent Traveling Wave Current Model and the Calculation of 3-D Pattern

The equivalent traveling wave current model of ridged horn antenna is proposed in the previous paper [22] presented by the authors' team. The reason of directional radiation of ridged horn antenna in broadband is explained preliminarily. The model is simple and easy to understand. However, only the E-plane and H-plane expressions of the equivalent traveling wave current model are calculated in [22],

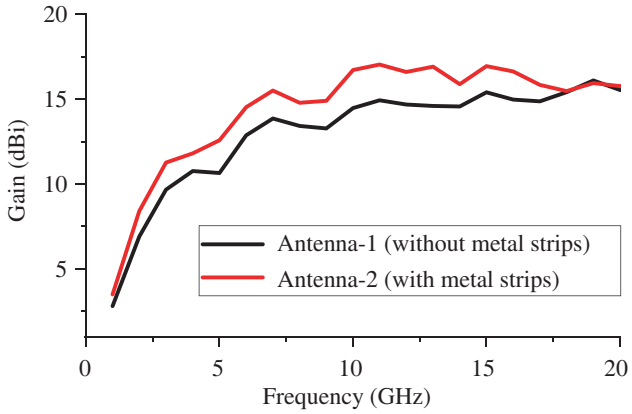

Figure 8. Comparison of gains between antenna-1 and antenna-2.

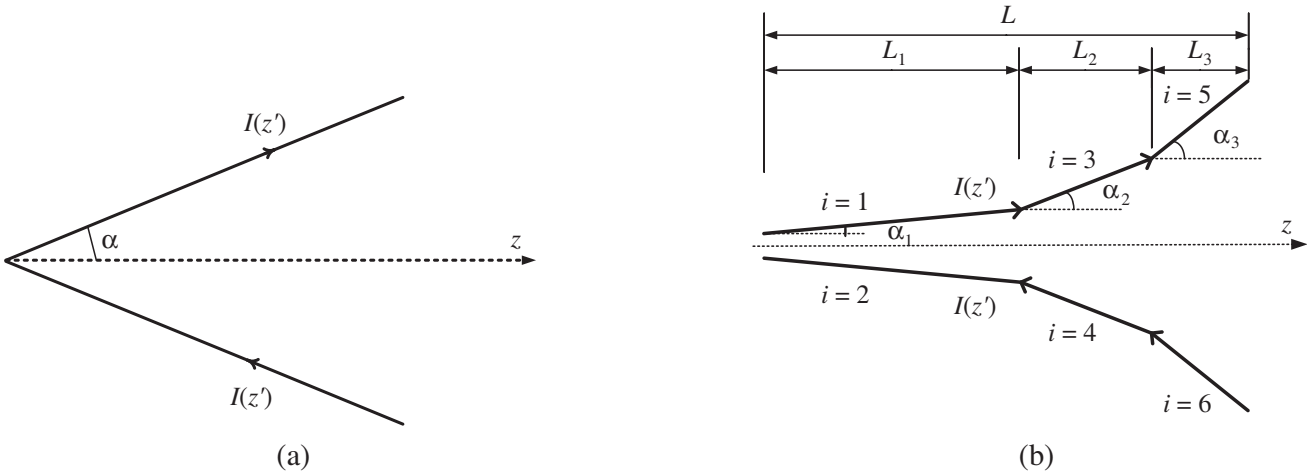

Figure 9. Two equivalent traveling wave current models. (a) Model in paper [22] (model-1). (b) Modified traveling wave current model in this paper (model-2).

and the 3-D expressions of patterns are not given. Moreover, the matching effect between patterns calculated by equivalent traveling wave current model in [22] and patterns simulated in CST becomes worse in the high frequency band. Therefore, in view of the problems of the model in paper [22] and considering the difference between the exponential ridge curve and the straight line, a modified equivalent traveling wave current model is proposed. And the 3-D expressions of radiation patterns are calculated by using the mathematical method of geometry based on the modified model.

As shown in Figure 9, model-1 is the equivalent traveling wave current model proposed in the previous paper [22], and model-2 is the modified equivalent traveling wave current model proposed in this paper. The angle relationship in the graph is $\alpha_1 < \alpha_2 < \alpha_3$, $\alpha = \alpha_2$. The improved model-2 is closer to the exponential curve of ridges. z' is a point on the curve, and its projection on the z-axis covers the range from 0 mm to 235 mm. The equation of the traveling wave current is: $I(z') = I_0 e^{-j\varsigma kz'}$, where I_0 is the amplitude of the current, and ζ is slow wave coefficient [22].

In order to calculate the 3-D patterns of the equivalent traveling wave current model, as shown in Figure 10, suppose that ON is a traveling wave current line; N point is in the first or second quadrant of yoz plane; the angle between ON and $+z$-axis is α; M is the observation point in space; the angle between OM and $+z$-axis is θ; the angle between OM and ON is Θ; M' point is the projection of M point on xoy plane. The angle between OM' and $+x$-axis is φ. When N point is in the first quadrant of yoz plane, it can be calculated:

$$\cos\Theta_1 = \cos\alpha\cos\theta + \sin\alpha\sin\theta\sin\varphi \tag{1}$$

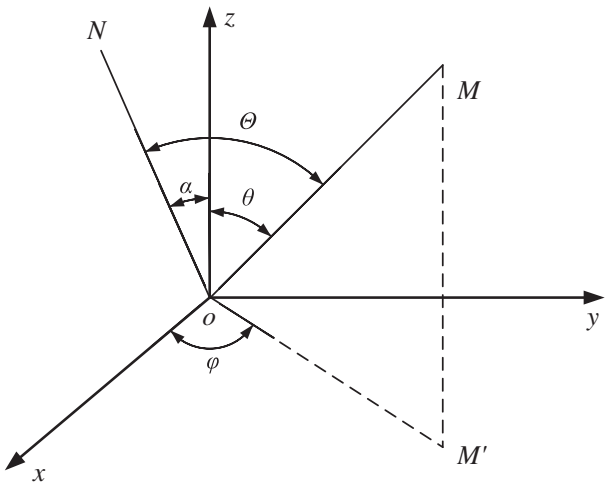

Figure 10. Schematic diagram of geometric structure relationship.

When N point is in the second quadrant of yoz plane, it can be calculated:

$$\cos\Theta_2 = \cos\alpha\cos\theta - \sin\alpha\sin\theta\sin\varphi \tag{2}$$

The radiation patterns' function of the traveling wave current line placed along the z-axis is:

$$F(\theta) = \left|\sin\theta\frac{e^{jkL(\cos\theta-\zeta)}-1}{\cos\theta-\zeta}\right| \tag{3}$$

Then the function of the pattern formed by the traveling wave current line with an angle of 2α (model-1) is:

$$\begin{aligned} F_1(\theta,\varphi) &= F(\Theta_1) + F(\Theta_2) = \left|\sin\Theta_1\frac{e^{jkL(\cos\Theta_1-\zeta)}-1}{\cos\Theta_1-\zeta} + \sin\Theta_2\frac{e^{jkL(\cos\Theta_2-\zeta)}-1}{\cos\Theta_2-\zeta}\right| \\ &= \left|\sqrt{1-\cos^2\Theta_1}\,\frac{e^{jkL(\cos\Theta_1-\zeta)}-1}{\cos\Theta_1-\zeta} + \sqrt{1-\cos^2\Theta_2}\,\frac{e^{jkL(\cos\Theta_2-\zeta)}-1}{\cos\Theta_2-\zeta}\right| \end{aligned} \tag{4}$$

For model-2, the expression of the 3-D pattern is:

$$F_2(\theta,\varphi) = \sum_{i=1}^{6} b_i F(\Theta_i) = \left|\sum_{i=1}^{6} b_i\sin\Theta_i\frac{e^{jk(a_iL)(\cos\Theta_i-\zeta)}-1}{\cos\Theta_i-\zeta}\right| \tag{5}$$

where b_i is the average value of current amplitude on the corresponding part of model-2, that is, the average value of current amplitude is extracted from the ridges in CST software; $\cos\Theta_i = \cos\alpha_{\frac{i+1}{2}}\cos\theta - \sin\alpha_{\frac{i+1}{2}}\sin\theta\sin\varphi$, $(i = 1, 3, 5)$; $\cos\Theta_i = \cos\alpha_{\frac{i}{2}}\cos\theta + \sin\alpha_{\frac{i}{2}}\sin\theta\sin\varphi$, $(i = 2, 4, 6)$.

The 3-D patterns calculated by model-1 and model-2 are drawn by MATLAB software at 18 GHz (the typical frequency in high frequency band). As shown in Figure 11, the 3-D patterns calculated by model-1 and model-2 and the 3-D pattern simulated (linear value) in CST of antenna-1 are displayed. The correlation coefficients calculated in the range of the main lobe are 0.26 (model-1 and the simulated pattern), 0.78 (model-2 and the simulated pattern), which proves that model-2 has better matching effect on antenna pattern than model-1, although its calculation is relatively complex. The calculation method of correlation coefficients is found in formula (6).

$$r(X,Y) = \frac{\mathrm{Cov}(X,Y)}{\sqrt{\mathrm{Var}[X]\mathrm{Var}[Y]}} \tag{6}$$

where $\mathrm{Cov}(X,Y)$ is the covariance of X and Y, $\mathrm{Var}[X]$ the variance of X, and $\mathrm{Var}[Y]$ the variance of Y. X is the matrix $A_{mn}(\theta,\varphi)$ corresponding to the normalized field strength of the 3-D pattern calculated

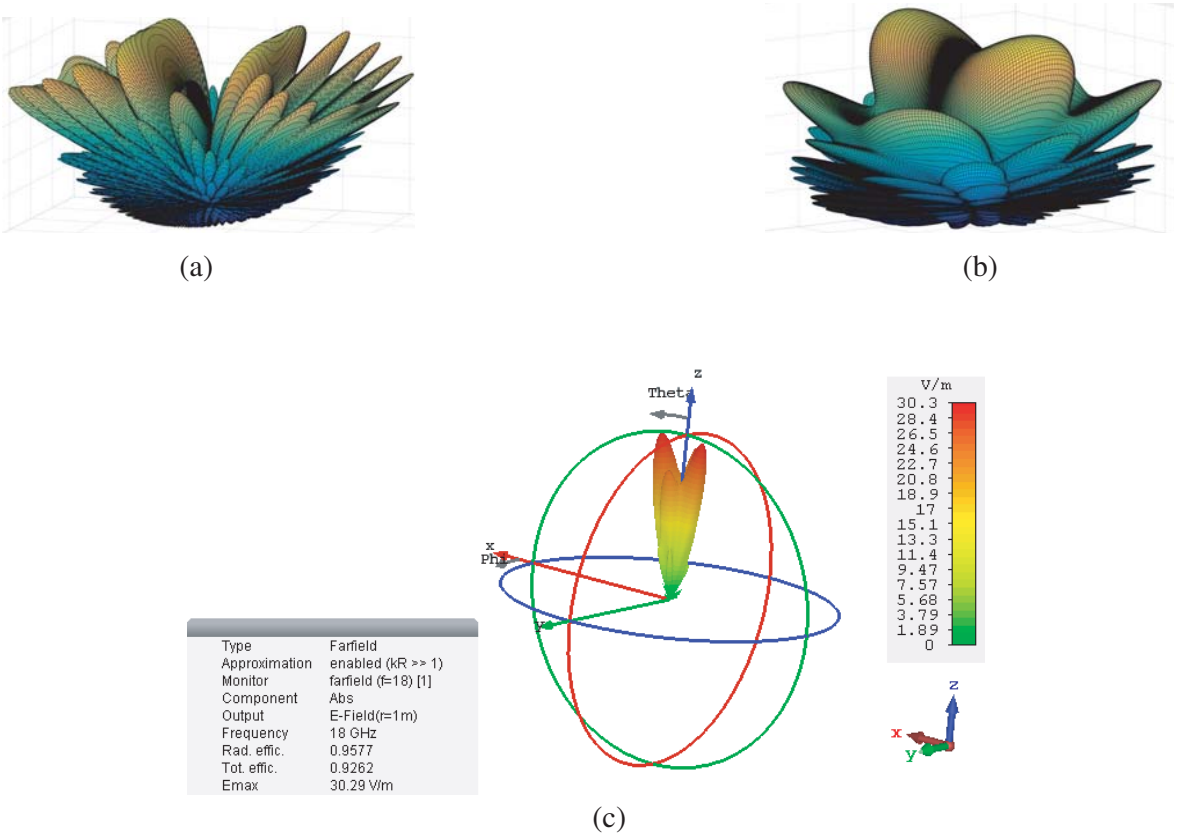

Figure 11. Comparison of 3-D simulated and calculated patterns (linear value) of electric field. (a) 3-D pattern calculated by model-1 at 18 GHz. (b) 3-D pattern calculated by model-2 at 18 GHz. (c) 3-D pattern simulated by CST at 18 GHz.

from model-1 or model-2, where $m = 45$, $n = 360$ (3-D pattern in the range of main lobe) or $m = 60$, $n = 1$ (H-plane pattern in the range of main lobe). Y is the matrix $B_{mn}(\theta, \varphi)$ corresponding to the normalized field strength of the 3-D pattern simulated in CST, where $m = 45$, $n = 360$ (3-D pattern in the range of main lobe) or $m = 60$, $n = 1$ (H-plane pattern in the range of main lobe).

3.2. Analysis of the Metallic Grip Sidewalls

3.2.1. Improvement of Matching Characteristics in Low Frequency Band

From the comparison of reflection coefficients given in Figure 6, it can be seen that the reflection coefficients of antenna-1 and antenna-2 are similar in high frequency band, but the matching performance of antenna-2 in low frequency band is better than those of antenna-1. Due to the introduction of metal strips, the minimum operating frequency is reduced from 1.7 GHz to 1 GHz. This phenomenon can be explained from the angle of resonance. Figure 12 shows the evolution process of equivalent circuit diagram.

When there are no metallic grid sidewalls, there is capacitance between the upper and lower sides of TEM ridged horn, and the capacitance per unit area is equivalent to:

$$\overline{C} = \frac{\varepsilon}{d} \tag{7}$$

The introduction of metallic grid sidewalls is equivalent to the introduction of inductance between the upper and lower sides of the horn, and the inductance per unit length is equal to:

$$\overline{L} = \frac{\mu_0}{2\pi}\left(\ln\frac{2l}{b+c} + \frac{1}{2}\right) \tag{8}$$

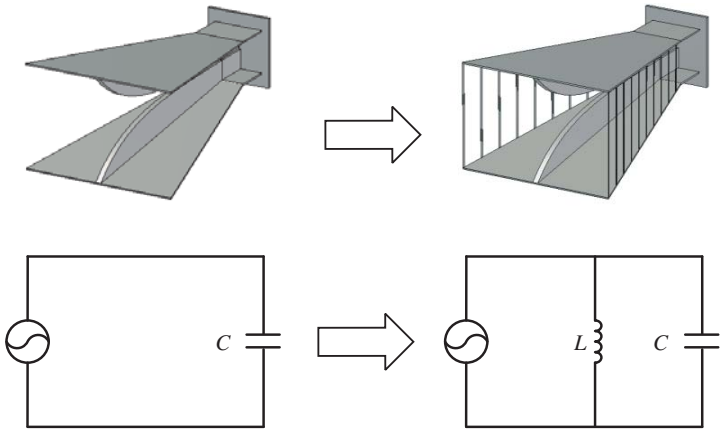

Figure 12. Evolution process of equivalent circuit diagram.

The resonant frequency can be calculated by formula (9):

$$f = \frac{1}{2\pi\sqrt{\widetilde{L}\widetilde{d}\widetilde{C}\widetilde{S}}} \tag{9}$$

where $\widetilde{d}$ is the average length of the metal strips, and $\widetilde{S}$ is the projection area of the upper and lower metal plates of the horn on the xoz plane.

The calculated resonant frequency is 1.20 GHz, which is close to f_0 (1.29 GHz) in Figure 6. The calculated result proves that the resonance of capacitance and inductance in low frequency band widens the operating bandwidth of the ridged horn antenna.

The classical inductance calculation method [23] is used to optimize the inductance at the feeding cavity, which improves the matching performance of the antenna. In this paper, the method is extended to the energy transmission part of the horn, that is, the metal strips on the sidewalls of the horn. The calculation and simulation results show that the method has a wide application range.

3.2.2. Suppressing the Splitting of Main Lobe in High Frequency Band

Figure 7 shows the comparison of patterns between antenna-1 (without metallic grid sidewalls) and antenna-2 (with metallic grid sidewalls). Due to the compensation radiation of the metal strips on the sidewalls of the horn, the splitting of patterns in high frequency band is well suppressed in antenna-2.

In order to analyze the influence of metal strips on radiation patterns, the following steps are adopted:

Step-1: The typical operating frequency is determined to be 9 GHz.

Step-2: The amplitude and phase distributions of surface current from the metal strips' center are extracted and plotted in Figure 13.

Step-3: The current phase difference between the longest strip and shortest strip in Figure 13 is calculated, and the result is 1980.0°.

Step-4: The distance between the center of the longest and shortest strips in Figure 5 is 194 mm.

Step-5: The phase shafting generated by traveling wave in free space at the distance of 194 mm is $\frac{0.194\,\mathrm{m}}{c/f} \times 360° = 2095.2°$, where $c = 3 \times 10^8$ m/s, $f = 9$ GHz.

Step-6: Comparing the phase differences in step 3 and step 5, the ratio of them is $\frac{1980.0°}{2095.2°} = 0.945$, which is close to 1. Therefore, the metal strips on antenna-2 prove to be traveling wave array.

Secondly, as shown in Figure 14, the current distribution on each strip of antenna 2 at 9 GHz is extracted. It can be seen that the phase distribution on each strip is approximately uniform, so the current on each metal strip is standing wave distribution, and the metal strips can be regarded as an array of dipoles.

Figure 15 shows the schematic diagram of the proposed traveling wave antenna array.

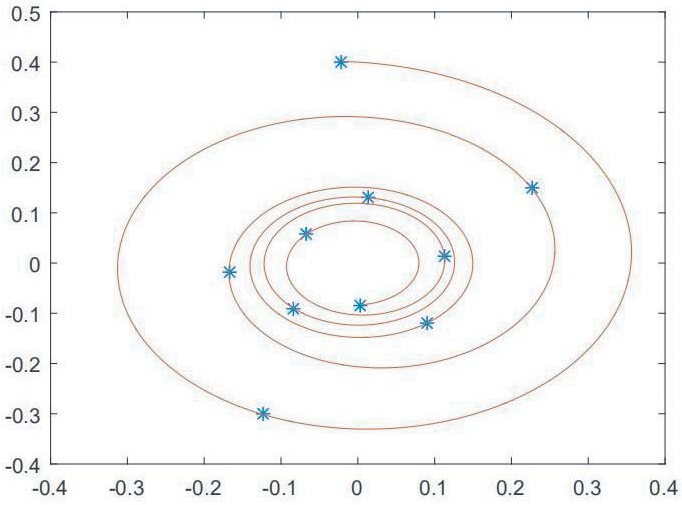

Figure 13. Amplitude and phase distributions of surface current at the center of every metal strips at 9 GHz.

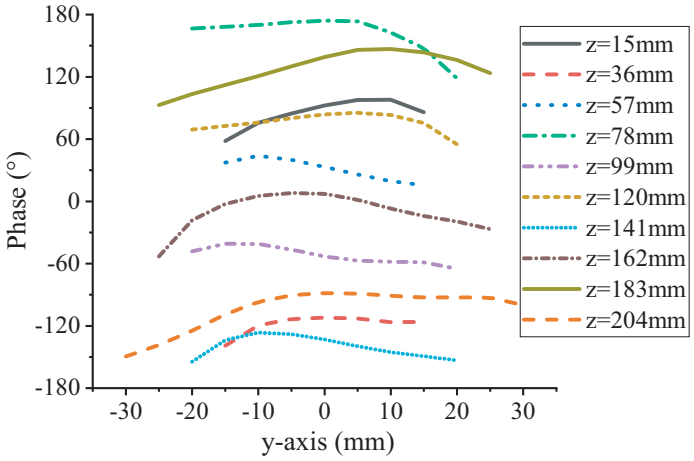

Figure 14. Phase distribution of surface current on every metal strips at 9 GHz.

The function of 3-D pattern calculated by the traveling wave antenna array is:

$$\begin{aligned} F_s(\theta,\varphi) &= \sum_{i=1}^{20} F_i = \sum_{i=1}^{20} \frac{60 I_i e^{j\xi_i}}{r_i} f_i(\theta,\varphi)\, e^{-jkr_i} \\ &\approx \frac{60}{r}\left[e^{-jkr_1}\sum_{i=1}^{10} I_i e^{j\xi_i} f_i(\theta,\varphi)\, e^{jk(r_1-r_i)} + e^{-jkr_{11}}\sum_{i=11}^{20} I_i e^{j\xi_i} f_i(\theta,\varphi)\, e^{jk(r_{11}-r_i)}\right] \\ &= \frac{60}{r}\left[e^{-jkr_1}\sum_{i=1}^{10} I_i e^{j\xi_i} f_i(\theta,\varphi)\, e^{jk(i-1)d\cos\delta} + e^{-jkr_{11}}\sum_{i=11}^{20} I_i e^{j\xi_i} f_i(\theta,\varphi)\, e^{jk(i-11)d\cos\delta}\right] \end{aligned} \quad (10)$$

where I_i is the magnitude of the current at the center of the strip; ξ_i is the phase of the current at the center of the strip; $f_i(\theta,\varphi) = \frac{\cos(kl_i\cos\tau)-\cos kl_i}{\sin\tau}$; τ is the angle between the distant observation point and the axis of dipole ($\cos\tau = \sin\theta\sin\varphi$); l_i is equal to the half of the metal strip's length; δ is the angle between the distant observation point and the axis of dipole array: $\cos\delta = \cos\beta\cos\theta + \sin\beta\sin\theta\cos\varphi$, $(i = 1, 2, ..., 10)$; $\cos\delta = \cos\beta\cos\theta - \sin\beta\sin\theta\cos\varphi$, $(i = 11, 12, ..., 20)$.

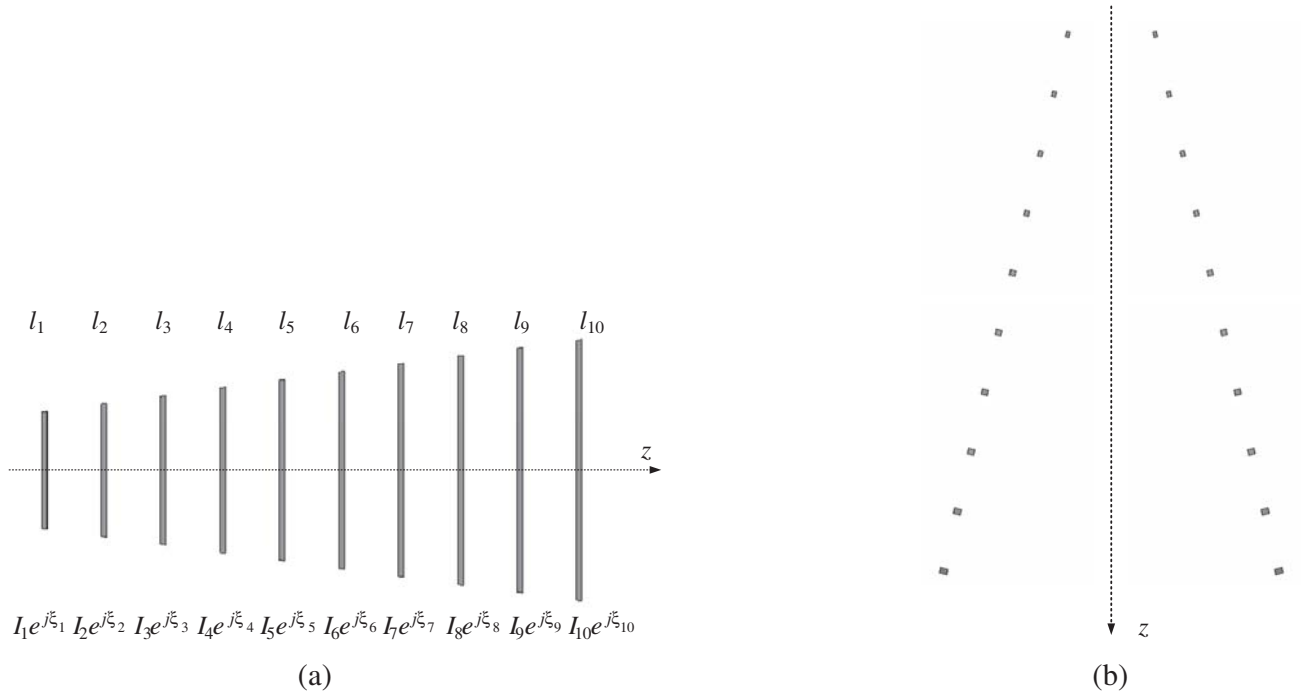

Figure 15. Schematic diagram of the proposed traveling wave antenna array. (a) Side view. (b) Top view.

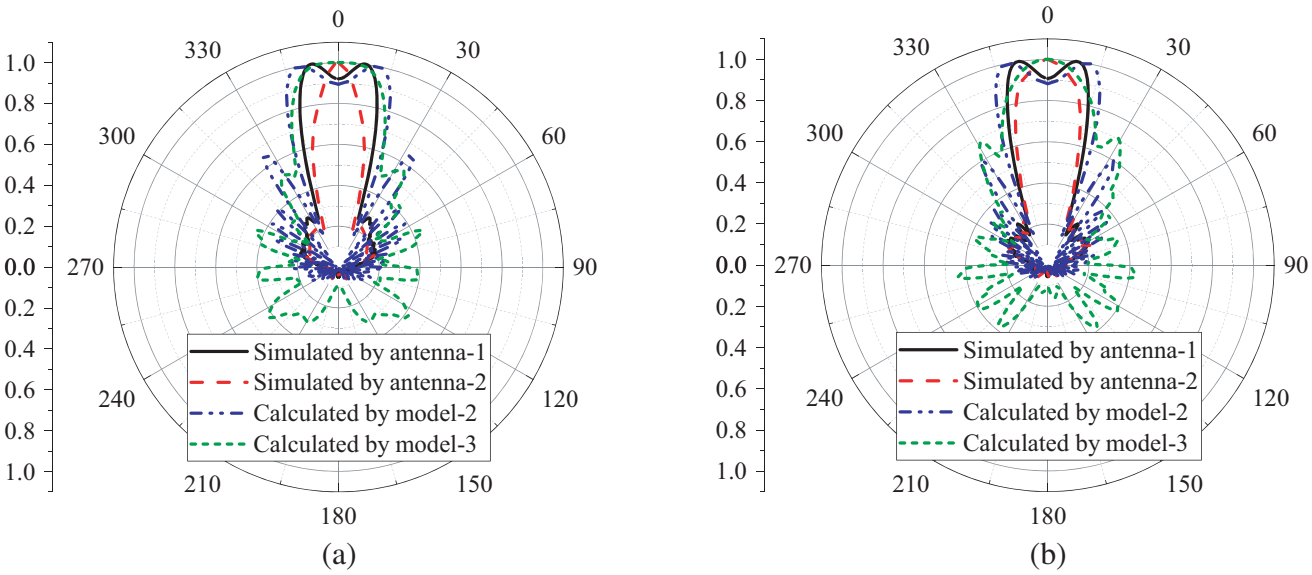

Figure 16. Comparisons between simulated and calculated results of pattern. (a) 16 GHz/H-plane. (b) 18 GHz/H-plane.

Model-3 is the combination of model-2 and traveling wave dipole array. The functions of radiation patterns calculated by model-3 are:

$$F_3(\theta,\varphi) = F_2(\theta,\varphi) + F_S(\theta,\varphi) \tag{11}$$

$$F_E(\theta,\varphi) = F_2(\theta,\varphi) + F_S(\theta,\varphi), \quad \theta = 90^\circ \tag{12}$$

$$F_H(\theta,\varphi) = F_2(\theta,\varphi) + F_S(\theta,\varphi), \quad \theta = 0^\circ \tag{13}$$

In order to verify the correctness of the proposed traveling wave dipole array, the H-plane patterns (normalized arithmetic value) calculated by model-2 and model-3 and the H-plane patterns (normalized arithmetic value) simulated by antenna-1 and antenna-2 are displayed in Figure 16. It can be seen that under the compensated radiation of traveling wave dipole array, the splitting of the main lobe of antenna pattern disappears. The correlation coefficients in the range of main lobe calculated by formula (6) are 0.82 (model-2 and antenna-1 at 16 GHz), 0.86 (model-2 and antenna-1 at 18 GHz), 0.94 (model-3 and antenna-2 at 16 GHz), and 0.98 (model-3 and antenna-2 at 18 GHz), respectively. The correctness of the proposed traveling wave dipole array is proved. The calculation results of model-3 and model-2 are in good agreement with the simulation results of antenna-2 and antenna-1, which proves the correctness of the proposed traveling wave dipole array.

It can be seen that the splitting of antenna patterns within the main lobe range has been greatly improved due to the introduction of metal strips. In model-3, an electric dipole array is introduced. Because the electric dipole array produces large radiation in the normal direction of the antenna aperture, the splitting of pattern main beam is greatly improved on one hand, while side lobes are produced in other directions on the other hand. Because the position of the side lobe is far from the normal direction of the antenna aperture, the model-3 proposed in this paper can successfully explain the mechanism that the introduction of metal strips can suppress the splitting of the main beam.

3.2.3. Enhancing Gains

As shown in Figure 8, the introduction of traveling wave dipole array is equivalent to the introduction of additional radiators, which enhances the gains of antenna when improving the matching characteristics in low frequency band and restraining the pattern splitting in high frequency band.

4. PROTOTYPE OF THE ANTENNA AND MEASURED RESULTS

As shown in Figure 17, the antenna is made of aluminum alloy and is measured in an echoic chamber, including reflection coefficients, gains, and radiation patterns. The overall size of the antenna is 240 mm × 140 mm × 94.6 mm. The coaxial line is used for feeding, and the axis of the coaxial line is parallel to the normal direction of the antenna aperture.

Figure 17. Prototype of the antenna.

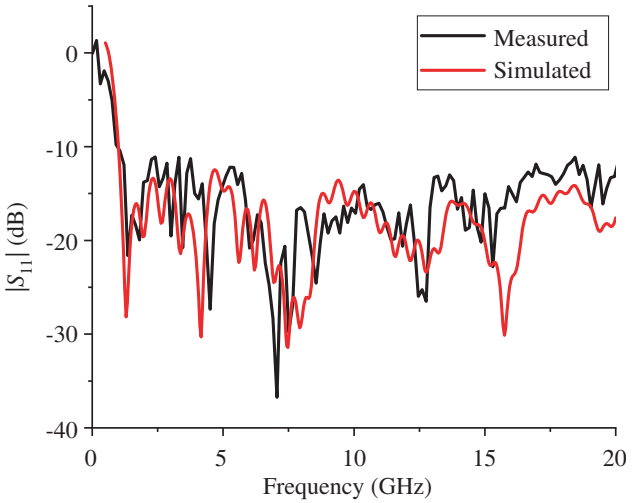

Figure 18. Comparison of reflection coefficients between simulation and measurement.

The reflection coefficients of the antenna are tested by Agilent N5227A vector network analyzer. As shown in Figure 18, the measured results indicate that the reflection coefficients are less than −10 dB in the frequency range of 1–20 GHz, which are in good agreement with the simulated results.

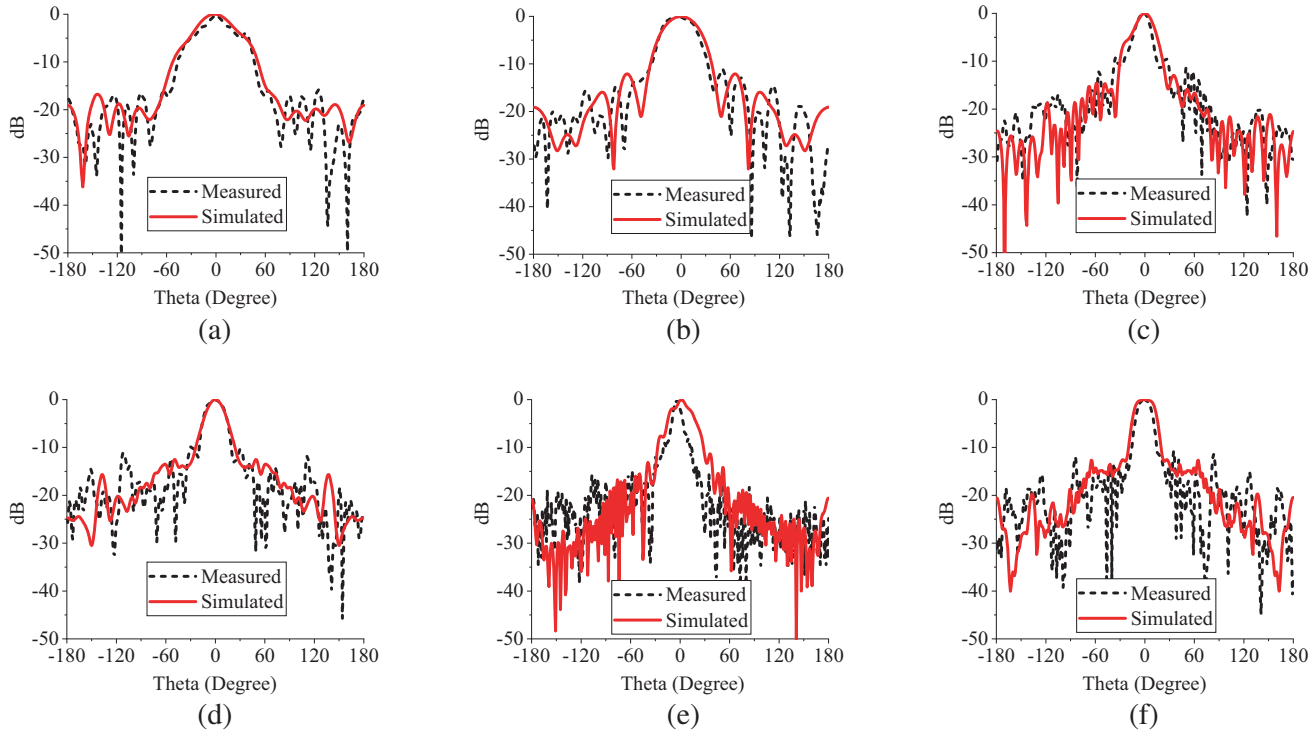

Figure 19. Comparison of patterns between simulation and measurement. (a) 2 GHz/E-plane. (b) 2 GHz/H-plane. (c) 9 GHz/E-plane. (d) 9 GHz/H-plane. (e) 18 GHz/E-plane. (f) 18 GHz/H-plane.

The comparison between simulated and measured results of radiation patterns is displayed in Figure 19. It can be seen that the measured normalized patterns at typical frequency in the frequency band agree well with the simulated results in the main lobe range. The main lobes of the measured patterns in high frequency are narrower than those of the simulated patterns, but remain convergent and non-splitting.

The comparison of gains between simulation and measurement is shown in Figure 20. It can be seen that the gains increase gradually with the variation of frequency, and there is no sudden drop of gains in the high frequency band. The test results are in good agreement with the simulation ones.

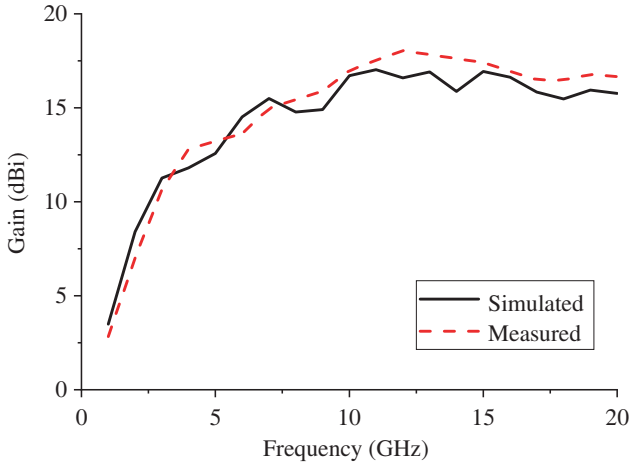

Figure 20. Comparison of gains between simulation and measurement.

5. CONCLUSION

An ultra-wideband ridged horn antenna with metallic grid sidewalls is designed, analyzed, and fabricated. The operating band is 1.0–20.0 GHz with the reflection coefficients less than −10 dB, and the relative bandwidth is as high as 180.95%. The gains are greater than 10 dBi in the frequency band of 2.6 to 20 GHz and greater than 16 dBi in the frequency range of 10–20 GHz with the gains fluctuation less than 1 dB. In the whole operating band, the radiation patterns radiate directionally along the normal direction of the horn aperture and do not split. Through the analysis of the antenna, the following conclusions can be drawn: (1) The modified multi-segment traveling wave current model-2 is closer to the ridge curve structure of exponential form and has better matching effect on antenna pattern; (2) The metal strips on the sidewalls of the horn are equivalent to the inductance structure. The resonance of the inductance and the capacitance between the upper and lower walls of the TEM horn in low frequency band improves the matching characteristic of the antenna in low frequency band and widens the bandwidth of the ridged horn antenna; (3) The metal strips on the sidewalls of the horn form a traveling wave dipole array, and the compensating radiation of the array restrains the splitting of the antenna pattern in high frequency band; (4) The compensating radiation produced by the metal strips on the sidewalls of the horn enhances the gains of the ridged horn antenna in the whole frequency band.

ACKNOWLEDGMENT

This work was supported in part by the Natural Science Foundation of Heilongjiang Province under Grant F2017011. The authors would also like to thank CST Ltd. Germany, for providing the CST Training Center (Northeast China Region) at our university with a free package of CST MWS software.

REFERENCES

1. Jacobs, O. B., J. W. Odendaal, and J. Joubert, "Quad-ridge horn antenna with elliptically shaped sidewalls," *IEEE Transactions on Antennas and Propagation*, Vol. 61, No. 6, 2948–2955, 2013.
2. Chen, Z., A. Mehdipour, and L. Matytsine, "Customized compact dielectric lens to improve double-ridge horn antenna performance for automotive immunity EMC test," *2016 IEEE International Symposium on Electromagnetic Compatibility (EMC)*, 835–840, Ottawa, 2016.
3. Schwarz, U., F. Thiel, F. Seifert, R. Stephan and M. A. Hein, "Ultra-wideband antennas for magnetic resonance imaging navigator techniques," *IEEE Transactions on Antennas and Propagation*, Vol. 58, No. 6, 2107–2112, 2010.
4. Zhang, F., M. Wang, L.-L. Yu, and J.-Y. Wu, "0.2 to 2.5 GHz advanced ultra-broadband double ridged horn antenna design and implementation," *Electronic Measurement Technology*, Vol. 41, No. 20, 68–72, 2018.
5. Manafi, S., M. Al-Tarifi, and D. S. Filipovic, "45–110 GHz quad-ridge horn with stable gain and symmetric beam," *IEEE Transactions on Antennas and Propagation*, Vol. 65, No. 9, 4858–4963, 2017.
6. Dehdasht-Heydari, R., H. R. Hassani, and A. R. R. Mallahzadeh, "A new 2–18 GHz quad-ridged horn antenna," *Progress In Electromagnetics Research*, Vol. 81, 183–195, 2008.
7. Lim, T. H., J. E. Park, and H. Choo, "Design of a vivaldi-fed hybrid horn antenna for low-frequency gain enhancement," *IEEE Antennas and Wireless Propagation Letters*, Vol. 66, No. 1, 438–443, 2018.
8. Botello-Perez, M., H. Jardon-Aguilar, and I. G. Ruiz, "Design and simulation of a 1 to 14 GHz broadband electromagnetic compatibility DRGH antenna," *2005 2nd International Conference on Electrical and Electronics Engineering*, 118–121, Mexico City, Mexico, 2005.
9. Abbas-Azimi, M., F. Arazm, and R. Faraji-Dana, "Design and optimization of a high-frequency EMC wideband horn antenna," *IET Microwaves, Antennas & Propagation*, Vol. 1, No. 3, 580–585, 2007.
10. Rodriguez, V., "Improvements to broadband dual ridge waveguide horn antennas," *2009 IEEE Antennas and Propagation Society International Symposium*, 1–4, Charleston, SC, 2009.

11. Amjadi, H. and F. T. Hamedani, "Ultra wideband horn antenna for microwave imaging application," *Proceedings of 2011 Cross Strait Quad-Regional Radio Science and Wireless Technology Conference*, Vol. 21, No. 5, 337–340, 2011.
12. Rodriguez, V., "New broadband EMC double-ridge guide horn antenna," *RF Design*, 44–50, 2004.
13. Lin, S., S. Yu, J. L. Jiao, and C. T. Yang, "Simulation and analysis of an ultra-wideband TEM horn antenna with ridge," *2017 International Symposium on Antennas and Propagation (ISAP)*, 1–2, 2017.
14. Wang, C., E. Li, Y. Zhang, and G. Guo, "Ridged horn antenna with adjustable metallic grid sidewalls and cross-shaped back cavity," *IEEE Antennas and Wireless Propagation Letters*, Vol. 15, 1221–1225, 2016.
15. Kuroptev, P. D., V. V. Levyakov, and A. V. Fateev, "Modified 0.6–50 GHz ultra-wideband double-ridged horn antenna design for parameters improvement," *2017 47th European Microwave Conference (EuMC)*, 1313–1316, 2017.
16. Dubrovka, F. F. and A. J. Sushko, "Improvement of characteristics of UWB double ridged horn antennas," *2010 5th International Conference on Ultra-wideband and Ultrashort Impulse Signals*, 45–47, 2010.
17. Amjadi, H. and F. T. Hamedani, "A novel 2–18 GHz TEM double-ridged horn antenna for wideband applications," *Proceedings of 2011 Cross Strait Quad-Regional Radio Science and Wireless Technology Conference*, 341–344, 2011.
18. Latif, S. I., D. Flores-Tapia, S. Pistorius, and L. Shafai, "Design and performance analysis of the miniaturised water-filled double-ridged horn antenna for active microwave imaging applications," *IET Microwaves, Antennas & Propagation*, Vol. 17, No. 2, 180–183, 2017.
19. Jacobs, B., J. W. Odendaal, and J. Joubert, "An improved design for a 1–18 GHz double-ridged guide horn antenna," *IEEE Transactions on Antennas and Propagation*, Vol. 60, No. 9, 4110–4118, 2012.
20. Bruns, C., P. Leuchtmann, and R. Vahldieck, "Analysis and simulation of a 1–18 GHz broadband double-ridged horn antenna," *IEEE Transactions on Electromagnetic Compatibility*, Vol. 45, No. 1, 55–60, 2003.
21. Nan, H., "Design and implementation of high performance UWB horn antenna," *2018 International Applied Computational Electromagnetics Society Symposium*, 1–2, 2018.
22. Lin, S., S. Liu, S. Yu, Y. Zhang, J. Jiao, and C. Yang, "Analysis of an ultra-wideband ridged horn antenna based on traveling wave current model," *2018 IEEE International Symposium on Antennas and Propagation & USNC/URSI National Radio Science Meeting*, 1079–1080, 2018.
23. Al-Zuhairi, D. T., J. M. Gahl, A. M. Abed, and N. E. Islam, "Characterizing horn antenna signals for breast cancer detection," *Canadian Journal of Electrical and Computer Engineering*, Vol. 41, No. 1, 8–16, Winter, 2018.